The AGN Outflow in the HDFS Target QSO J2233-606: Analysis of a High S/N VLT/UVES Spectrum

Jack R. Gabel, Nahum Arav (CASA/University of Colorado) & Tae-Sun Kim (IoA/Cambridge)

Overview

- Detailed constraints on the physical conditions, chemical abundances and geometry of the intrinsic absorption systems ($v \approx -5000 - -4000$ km s^{-1}) in QSO J2233-606 are derived using a 14 hour VLT/UVES observation.
- A velocity-resolved, global fitting of the combined CNO lithium-like doublets and Lyman series lines allows treatment of complex nuclear geometry in the $C - N_{ion}$ solution, revealing: the outflow fully (or nearly) occults the continuum, with lower coverage of the BLR in all components; the BLR covering factor increases with increasing outflow velocity; kinematic substructure is present in the ionic column density profiles.
- A new velocity-dependent photoionization modeling technique is applied, making use of the highly-resolved profiles to increase constraints, thereby allowing precision measurement of the outflow's chemical abundances and velocity-dependent model parameters (U,N_H). This reveals: the outflow systems are super-solar ($\approx 4Z_\odot$), with an over-abundance of N consistent with Z^2 scaling; velocity-dependent ionization structure, with relatively high-ionization material present just redward of the strong components.

Intrinsic UV Absorption in the UVES Spectrum

The bright quasar QSO J2233-606 (B =17.5; z =2.238) was selected as the central target in the STIS field of the Hubble Deep Field South (HDFS) observations. Intrinsic UV absorption components representing mass outflow systems at radial velocities $v \approx -5000 - -3800$ km s^{-1} were identified in ground-based observations based on partial line-of-sight covering factors, relatively broad widths, and proximity in redshift to the quasar host galaxy (Petitjean & Srianand 1999). J2233 was observed with VLT/UVES for a total of 50 ks as part of a large IGM program (Kim et al. 2001), yielding a high S/N ($\approx 25 - 50$), high-resolution ($R \approx 30{,}000 - 50{,}000$) spectrum uniformly spanning key diagnostic UV lines. Key features of the spectrum:

- Three strong kinematic components are detected at $v_r \approx -4800$, -4150, and -3950 km s^{-1} (components 1, 2 and 3, respectively), exhibiting absorption in increasing strength in the C IV, N V, and O VI doublets; lower ionization lines (C III and Si IV) are not detected.
- Lyα is present in all three components; Lyβ is detected in component 1, has a potential weak feature in component 2, but is contaminated with intervening Lyα forest absorption in component 3.
- Three additional systems are seen only in the O VI doublet, just redward of component 3 ($v_r \approx -3850$, -3700, and -3625 km s^{-1}).

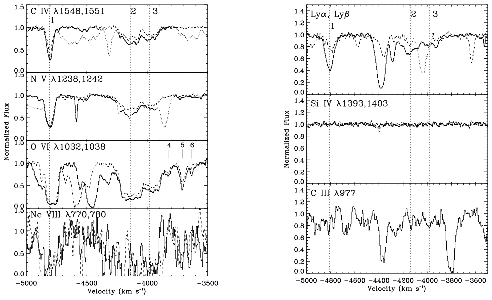

Figure 1. Normalized absorption profiles from VLT/UVES spectrum of QSO J2233-606. The Ne VIII doublet from the HDFS E230M observations is also included. Long wavelength doublet members and Lyβ are plotted with dashed lines, short wavelength doublet lines and Lyα with solid lines. Dotted vertical lines denote the three strong kinematic components analyzed in this study; tick marks show the three additional components seen only in O VI and Ne VIII. Contaminated regions are plotted with dotted lines.

Velocity-Dependent $N_{ion} - C$ Solutions

Background: Deconvolving the effects of line-of-sight covering factor (C) and optical depth (τ) [e.g., Hamann et al. (1997)] is crucial for obtaining ionic column densities for interpreting AGN outflows and gives unique geometrical constraints. This may be complicated by the complex nuclear geometry of the background emission sources the absorption is imprinted on: e.g., different spatial scales and geometry of continuum and emission-line regions (Ganguly et al. 1999; Gabel et al. 2003; Scott et al. 2004) – the traditional solution using a single doublet pair cannot treat this.

Formalism: Thus, we applied a global fitting approach to determine C and N_{ion} treating individual covering factors for the BLR and continuum source by simultaneously fitting all observed lines. This involved optimization fitting of the set of absorption equations giving the normalized intensity of the j^{th} line:

$$I^j = \Sigma_i [R_i^j (C_i^j e^{-\tau^j} + 1 - C_i^j)], \qquad (1)$$

where the i^{th} individual emission source contributes a fraction $R_i^j = I_i^j / \Sigma_i [I_i^j]$ to the total intrinsic intensity and has covering factor C_i^j (e.g., Ganguly et al. 1999). Different ions were linked in the solution by assuming they all share the same continuum and BLR covering factors (C_c, C_l), giving up to 8 detected lines (where Lyβ is not contaminated, Figure 1) to solve for the two covering factors and four column densities. Independent solutions were derived in each velocity bin via the Levenberg-Marquardt non-linear least-squares minimization technique; profile fits from these solutions are in Figure 2.

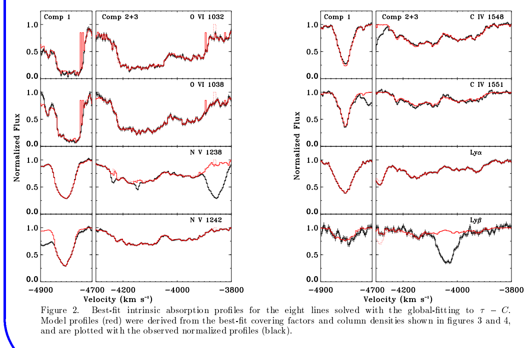

Figure 2. Best-fit intrinsic absorption profiles for the eight lines solved with the global-fitting to $\tau - C$. Model profiles (red) were derived from the best-fit covering factors and column densities shown in figures 3 and 4, and are plotted with the observed normalized profiles (black).

Results: Figures 3 and 4 show best-fit covering factors and optical depths:

- There is a trend of increasing covering factor for components with greater outflow velocity: component 1 occults the entire continuum source and ≈55% of the BLR; component 2 covers the continuum source, but little or none of the BLR; component 3 only partially covers the continuum source (≈70%).
- Narrow kinematic substructure in the ionic column densities is present: the red-wing of component 1 is highly ionized, having saturated O VI and weak absorption from lower ionization species compared with the core of this component; components 2 and 3 break down into a series of subpeaks in τ.

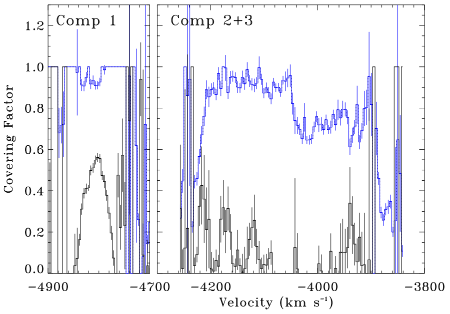

Figure 3. Global-fit solution to the line-of-sight absorption covering factors. BLR covering factors are plotted with black histograms, continuum covering factors are in blue.

Since the τ solutions to the different ions are not independent in this analysis, we also measured each doublet pair and the Lyα-Lyβ pair independently, allowing for ion-dependent covering factors. Here, C_c in each kinematic component was fixed to the mean value from the global fit (Figure 3), and τ and C_l were solved using χ^2 analysis. Results are shown in Figure 4 (red) for comparison.

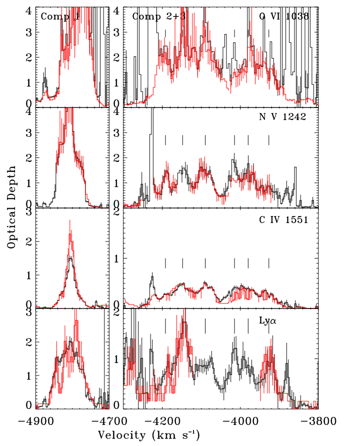

Figure 4. Global-fit solutions to the intrinsic absorption optical depth profiles. Tickmarks show peaks in the narrow substructure seen in components 2 and 3. To test the effect of ion-dependent covering factors, solutions for the individual doublet and Lyα - Lyβ pairs keeping C_c fixed to its mean value derived in each kinematic component (Figure 3) are shown for comparison (red).

A New Modeling Technique: Velocity-Dependent Photoionization Models for Precision Abundance Measurements

To fully model the measured C IV, N V, O VI, and H I columns, five parameters must be specified: the ionization parameter ($U = Q/4\pi R^2 n_H c$), total column density (N_H), and the abundances of C, N, and O relative to H; thus the solution for a single measurement of these ions is underconstrained. **We employed velocity-dependent photoionization modeling, utilizing the high-resolution to give additional constraints and thereby obtain the full solution of the abundances and physical conditions.** Measured column densities in *each velocity bin* were compared with a grid of photoionizaton models in U,N_H; solutions at different velocities were linked by requiring the metal abundances to be identical across the profiles of each kinematic component.

- free parameters: U, N_H in each of the n_v velocity bins; C, N, and O abudandces: $2 \times n_v + 3$ free parameters
- constraints: n_{ion} ionic column densities (up to four, depending on contamination or saturation) in each velocity bin: $\Sigma_{i=1,n_v} n_{ion;i}$ constraints
- best-fit solutions: the set of velocity-dependent U, N_H values and the C, N, and O abundances that minimize χ^2 from:

$$\chi^2 = \Sigma_i \Sigma_j [\frac{N_{obs;j,i} - N_{mod;j}(U, N_H) f_j}{\sigma_{j,i}}]^2, \qquad (2)$$

where the measured column density of the j^{th} ion in the i^{th} velocity bin $N_{obs;j,i}$ is compared with the model column densities from the grid $N_{mod;j}$, f_j is the scale factor relative to solar abundances, and $\sigma_{j,i}$ the measurement uncertainty.

Results: Components 1–3 were fit individually with this method:

- All kinematic components have supersolar metal abundances, with consistent results for each element in each component (see Figure 5). The analysis gives [C/H] and [O/H] ≈0.5 – 0.6, and [N/H] ≈ 1.2, consistent with the Z^2 scaling of N predicted from secondary CNO nucleosynthesis.
- The lowest ionization material in each of components 1 – 3 has similar ionization ($\log(U) \approx -1.2$). Higher ionization gas is required at the same velocities to account for the Ne VIII absorption (shown also by Petitjean 1999). The redwing of component 1, and components 4 – 6 which lie just redward of component 3, have ionization parameters at least 5 – 10 times greater than the low-ionization component 1 – 3 gas.

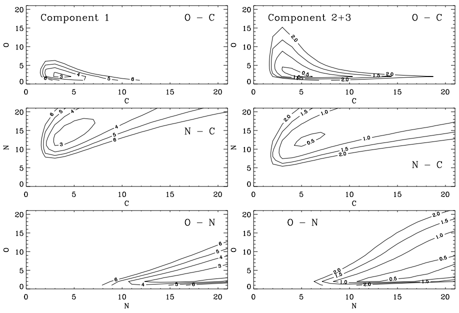

Figure 5. C, N, O abundance solutions from velocity-dependent photoionization modeling for component 1 (left) and components 2+3 (right). The 2-D contour projections of the 3-D reduced χ^2 volume are shown for each C-N-O plane. For each 2-D projection, the abundance of the third, perpendicular element was held fixed at its best-fit value.

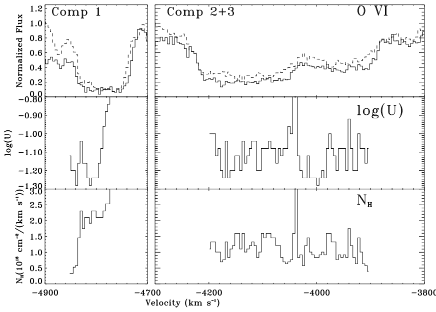

Figure 6. Velocity-dependent photoionization model solutions. The best-fit solutions are shown for the ionization parameter (middle panel) and total H column density (bottom), with metal abundances shown in figures 5 and 6. The O VI doublet profiles are shown in the top panel for reference.

Implications and Conclusions

- Velocity-dependent photoionization modeling of resolved absorption provides a powerful new probe of chemical abundances and kinematic structure in the physical conditions.
- Chemical enrichment: The finding of super-solar abundances in the outflow in J2233 and associated absorbers in other distant QSOs (e.g., Hamann & Ferland 1999; D'Odorico 2004) supports the evolutionary scenario of most chemical enrichment occurring in massive nuclei before at least $z \gtrsim 2$–3. A subsequent or coeval QSO phase may then distribute the enriched gas to the host galaxy and IGM via an outflow.
- Kinematic-geometric structure: The $C_l - v$ trend may indicate the absorber size (projected transversely) increases with outflow velocity. If the radial size scales with v as well, the similar N_H and U for the lowest-ionization material in components 1 – 3 implies their distances increase with outflow velocity.
- Clustering of narrow components: The kinematic clustering of narrow components and resolved substructure in J2233 is commonly seen in QSO outflows. This suggests we are seeing a number of distinct, related absorption regions in our sightline (continuous stream lines or distinct clouds). There may be a continuous distribution of absorption widths associated with AGN outflows, ranging from J2233 to the classical BAL troughs, perhaps related to the orientation of our sigthline to the nucleus.

References

Gabel, J. R., et al. 2005, ApJ, 623, 85
Ganguly, R., Eracleous, M., Charlton, J. C., & Churchill, C. W. 1999, AJ, 117, 2594
Hamann, F. & Ferland, G. 1999, ARA&A, 37, 487
Hamann, F., Barlow, T. A., Junkkarinen, V., & Burbidge, E. M. 1997, ApJ, 478, 80
Kim, T.-S., Cristiani, S., & D'Odorico, S. 2001, A&A, 373, 757
Petitjean, P. & Srianand, R. 1999, A&A, 345, 73
Scott, J., et al., 2004, ApJS, 152, 1